Ordered mesoporous carbons obtained by soft-templating of tannin in mild conditions

Angela Sanchez-Sanchez, Maria Teresa Izquierdo, Ghouti Medjahdi, Jaafar Ghanbaja, Alain Celzard, Vanessa Fierro

Ordered mesoporous carbons obtained by soft-templating of tannin in mild conditions

A. Sanchez-Sanchez [a,*], *Maria Teresa Izquierdo* [b], *Ghouti Medjahdi* [c], *Jaafar Ghanbaja* [c], *Alain Celzard* [a], *Vanessa Fierro* [a,*]

[a] Institut Jean Lamour, UMR CNRS-Université de Lorraine n°7198, ENSTIB, 27 rue Philippe Séguin, BP 21042, 88051 Epinal Cedex 9, France.

[b] Instituto de Carboquimica, ICB-CSIC, Miguel Luesma Castan, 4, 50018 Zaragoza, Spain.

[c] Institut Jean Lamour, UMR CNRS-Université de Lorraine n°7198, Parc de Saurupt, CS 50840, 54011 Nancy Cedex, France.

KEYWORDS. Tannin, surfactant, soft-templating, self-assembly, supercapacitor.

ABSTRACT

We show that soft-templating synthesis of biosourced OMCs under rather mild pH conditions is possible by controlling the reaction temperature, without using either formaldehyde or toxic phenolic reagents. Removal of the surfactant at 400°C and subsequent carbonisation at 900°C allows reducing the shrinkage and preserving the material mesoporosity. Self-assembly of mimosa tannin with Pluronic® F127 in mild conditions (30°C, pH 3) leads to hierarchical OMCs with more developed porosities, more ordered mesostructures and higher nanotexture ordering than under more acidic conditions that are commonly used in soft-templating of OMCs. Further development of the OMC porosity by physical activation with CO_2 increased the micropore volume by ~60% without significantly affecting the structural ordering, but decreased the mesopore volume and the oxygen content whereas the PSD was slightly widened in the mesopore range. The activated OMC exhibited high gravimetric capacitances of 286 F g^{-1} (determined by cyclic voltammetry), a high capacitance retention of 50% at 12 A g^{-1} (determined by galvanostatic charge-discharge), high energy and power densities of 17.54 W kg^{-1} and 16.29 kW kg^{-1}, respectively, and a faster frequency response, 4.39 seconds, than the non-activated OMC, making it a more appropriate material for practical supercapacitors.

1. Introduction

Since their discovery, ordered mesoporous carbons (OMCs) have attracted considerable interest due to their unique properties, such as high surface areas, large pore volumes and uniform mesopores with controlled size and shape [1–3]. Their 3D nano-sized frameworks indeed produce quantum effects at the nanoscale that allow attaining unusual electrical, mechanical and optical properties. Uniform mesoporous channels also facilitate the transport of ions, atoms and large molecules through the material bulk to active sites [3–5]. As a result, OMCs have been successfully applied in many fields, including catalysis [6,7], separation [9,10], environmental remediation [11,12] or energy conversion and storage [13–16].

Supercapacitors are electronic devices that can store energy at the electrode/electrolyte interface both physically, by ion accumulation forming the electric double layer, and chemically, through Faradaic reactions of the surface functional groups [17,18]. They exhibit high reversibility, long life cycle and high power density, and they are mainly applied for providing short-term pulses in hybrid vehicles or as uninterruptible power supplies [19]. Many works have demonstrated that using electrodes based on OMCs possessing well-balanced micro / mesoporosity or hierarchical structures enhances the supercapacitor performance in terms of rate capability and cycling stability, both of them being important properties for practical devices. Thus, micropores with adequate pore diameter provide active surface and play a key role for ion adsorption while mesopores favour quick transport of ions towards micropores [20].

Hard-templating, or nanocasting, is one of the most used techniques for preparing hierarchical OMCs. It allows controlling shape and size of pores, as well as the wall thickness, by selecting adequate templates, usually mesoporous silica [3,21]. However, the procedure is expensive and

time-consuming, and the need to remove the silica template, generally by HF leaching, prevents its use for manufacturing OMCs at large scale.

Successful preparation of OMCs by soft-templating requires several conditions that are not easy to meet at the same time, such as micelle formation capability of the structure-directing copolymer, interactions between the copolymer units and the functional groups of the precursor, and crosslinking capability and thermal stability of the carbon precursor. Due to the high formation energy of C-C linkages and the limited number of precursors fulfilling the aforementioned requirements, the synthesis of OMCs by soft-templating is a complex issue [22]. Soft-templated OMCs exhibiting narrow pore size distributions (PSDs) and surface areas as high as ~ 1400 $m^2 g^{-1}$ have been prepared from phenolic resin monomers such as phenol, resorcinol or phloroglucinol, using formaldehyde as cross-linker, Pluronic® triblock-copolymers as soft-templates, and water or water/alcohol mixtures in acidic medium as solvent [23,24]. Since formaldehyde and most synthetic phenolic molecules are highly toxic, expensive and non-renewable chemicals, their substitution by cheap, environment-friendly and renewable precursors is highly desired. Thus, hexamethylenetetramine (HMT) has been suggested as alternative crosslinker, since it is poorly volatile but still yields formaldehyde and ammonia upon hydrolysis. Mesoporous carbons exhibiting either 3D-cubic or wormlike, or 2D-hexagonal structures could indeed be prepared from HMT, resorcinol (R) and furfural (F) as carbon precursors and F127 as surfactant, by modulating the F127 / RF ratio [25]. Phenolic monomers could also be substituted by biosourced polymers or oligomers such as lignin or condensed tannins, respectively. For instance, Saha et al. prepared OMCs by soft-templating of lignin with Pluronic® F127, but those materials exhibited less developed porosities and wider PSDs than OMCs prepared from phenol in similar conditions [26]. As a matter of fact, lignin possesses a

highly branched, complex structure and a low reactivity, both preventing its proper self-assembly with the surfactant micelles. In contrast, condensed tannins are non-toxic and cheap bio-oligomers obtained from a variety of tree barks (chestnut, mimosa, pine, etc.), whose chemical structure consists of polycondensed flavonoid units, i.e., with 4 to 6 –OH groups located on two aromatic rings [27], able to undergo similar chemical reactions as phenol or resorcinol. OMCs exhibiting either lamellar or 2D-hexagonal structures and having various pore sizes and surface areas have thus been successfully prepared from chestnut tannin or mimosa tannin and Pluronic® F127 by modulating the experimental conditions [28,29]. However, no control of the temperature during the oligomer-surfactant assembly, a critical step in soft-templating synthesis, was exerted, and highly acidic media were necessary to ensure the proper formation of the surfactant-oligomer supramolecular structure. Highly acidic conditions require the use of corrosion-resistant equipment and consistent security measures, which is detrimental for industrial manufacturing purposes. Thus, using milder acidic conditions to synthesise OMCs by soft-templating should be very interesting from the operational point of view.

In the present study, we synthesised hierarchical OMCs by soft-templating of mimosa tannin with Pluronic® F127 surfactant in aqueous solution. Both the pH and the temperature of the assembly step were controlled, and the soft-template was removed at moderate temperature for better preserving the ordered structure of the materials. Physical activation with CO_2 was also applied to develop further the microporosity of one of those hierarchical OMCs. The influences of the medium pH and of the assembly temperature on the development of porosity and the resultant physicochemical properties of the resultant OMCs were investigated. Finally, some of the obtained OMCs were tested as supercapacitor electrodes, and the electrochemical

performances in 2 mol L^{-1} H_2SO_4 aqueous electrolyte were correlated to their physicochemical properties.

2. Experimental section

2.1. Materials

Pluronic® F127 (average molecular weight 12.6 kDa), hydrochloric acid (37% in water), sodium hydroxide (98%), and acetylene carbon black powder (< 100 nm) were purchased from Sigma–Aldrich. Sulphuric acid solution (2 mol L^{-1}) was prepared from a concentrated sulphuric acid solution (95–98%) supplied by Sigma–Aldrich. Mimosa tannin was provided under the name FINTAN OP and was kindly supplied by the company SilvaChimica (St. Michele Mondovi, Italy). Polytetrafluoroethylene (PTFE) and glass fibre separator were provided by Aldrich and Pall Life Sciences, respectively. All the materials were used as received.

2.2. Synthesis of the ordered mesoporous carbons (OMCs)

Figure 1 illustrates the different steps of the soft-templating route used here to obtain the OMCs:

1) *Mixture of tannin and surfactant aqueous solutions and auto-assembly of the mixture at controlled temperature*: the mimosa tannin solution (2 g in 16 mL of water), adjusted at a certain pH between 1 and that of tannin in water, i.e., without pH adjustment (between 4.50 and 4.65), was added to the Pluronic® F127 solution (2 g in 16 mL of water). The tannin / surfactant mixture was left for auto-assembly at controlled temperature (10, 20 or 30°C) for 72 h. During this time, tannin molecules interacted with F127 micelles and self-organised around them, giving rise to an ordered supramolecular structure.

2) *Phase separation*: After 72 h, the flask was kept at room temperature (20°C, 5 days) until complete phase separation. Next the supernatant, containing water and non-reacted molecules, was removed while the heavier phase at the bottom, containing the surfactant-tannin supramolecular complex, was dried at 60°C under vacuum.

3) *Removal of the surfactant template*: The dried solid was carbonised in a two-step procedure under nitrogen flow (80 mL min^{-1}): (i) a first step to gently remove the surfactant (heating rate 1°C min^{-1} up to 400°C; 4 h dwell time), and (ii) a second step to carbonise the material (heating rate 2°C min^{-1} up to 900°C; 1 h dwell time). The temperature steps were deduced from thermogravimetry (TG) results, as explained below. The resultant OMCs were labelled Fi/T, where i indicates the initial pH of the tannin solution (4.5 for the sample at the pH of tannin in water, without HCl added) and T is the temperature of the assembly step. The carbonisation yield, η (%), was determined as the mass ratio of dry surfactant–tannin composite material (i.e., before pyrolysis) to carbon (i.e., after pyrolysis).

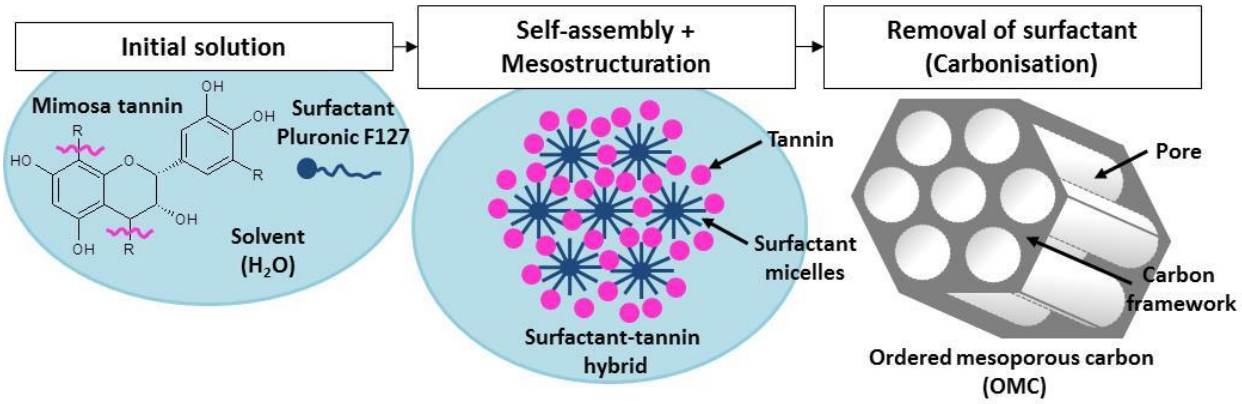

Figure 1. Schematic representation of the soft-templating method used to synthesise OMCs.

2.3. Synthesis of the activated OMC

F3/30 carbon was heated in nitrogen flow (80 mL min^{-1}) up to the selected activation temperature (900°C, 2°C min^{-1}). Once the target temperature was reached, CO_2 was forced to flow (50 mL min^{-1}) throughout the sample (2 h), which was subsequently cooled down to room temperature in nitrogen flow (80 mL min^{-1}). The obtained OMC was labelled C3/30.

2.4. Characterisation

2.4.1. Physicochemical characterisation

Nitrogen adsorption–desorption isotherms were obtained at -196°C using a Micromeritics ASAP 2020 automatic system, whereas carbon dioxide adsorption isotherms were acquired at 0°C with a Micromeritics ASAP 2420. The surface areas were calculated by applying: (i) the BET equation to the nitrogen isotherms in the relative pressure interval wherein the BET constant is positive, leading to A_{BET} (**m^2 g^{-1}**); and (ii) the Non-Local Density Functional Theory (NLDFT, SAIEUS software) to both nitrogen and carbon dioxide isotherms, leading to S_{NLDFT} (**m^2 g^{-1}**) [30]. The pore size distributions (PSDs) of the carbon materials were obtained by applying the Barret–Joyner–Halenda (BJH) method with the Kruk–Jaroniec–Sayari (KJS) correction to the desorption branch of the nitrogen isotherms. The total pore volumes, V_T (cm^3 g^{-1}), were calculated as the amounts of nitrogen adsorbed at a relative pressure of 0.98. The micropore volumes were calculated by applying the Dubinin-Radushkevich (DR) equation: (i) to nitrogen adsorption isotherms, leading to $V_{\mu\text{-}N2}$ (cm^3 g^{-1}); and (ii) to carbon dioxide isotherms, leading to $V_{\mu\text{-}CO2}$ (cm^3 g^{-1}). The micropore volume was also calculated by applying the NLDFT method (SAIEUS software) to both the nitrogen and carbon dioxide isotherms, giving rise to $V_{\mu\text{-}NLDFT}$. The mesopore volumes, V_M (cm^3 g^{-1}), were calculated by subtracting $V_{\mu\text{-}NLDFT}$ from V_T.

The thickness of the carbon wall, *t* (nm), was calculated as the difference *a* – *w*, where *a* is the unit cell parameter of the ordered structure determined from the XRD patterns, and *w* is the main pore size obtained from the BJH-KJS distributions.

For each sample, the carbonisation yield was determined as the mass ratio of dry surfactant–tannin composite material before pyrolysis to carbon after pyrolysis. For the activated material, the activation yield was calculated as the ratio: mass of carbon material before activation to mass of activated carbon after activation.

In order to determine in which temperature interval the surfactant can be removed from the surfactant–tannin composite, the thermal decomposition of the latter was studied with a STA 449F3 Jupiter (NETZSCH) microbalance by heating the sample under argon flow (40 mL min^{-1}) up to the final temperature (900°C, heating rate 2°C min^{-1}).

Small-angle X-ray diffraction (XRD) patterns of carbons were recorded with a Panalytical X'Pert Pro diffractometer. The latter was equipped with a Cu (Kα radiation) anticathode and a high-speed multichannel X'Celerator detector (scanning range 2θ = 0.5–3°; step size = 0.01671°; time per step size 1.26 s), and was used in a Bragg–Brentano configuration in reflection mode. The unit cell parameter (*a*, nm) of the carbon mesostructures was calculated by applying Equation (1):

$$\boldsymbol{a} = \frac{\mathbf{2}\,\boldsymbol{d_{100}}}{\sqrt{\mathbf{3}}} \qquad (1)$$

where d_{100} (nm) is the interplanar spacing obtained from XRD patterns.

Raman spectra were obtained with a Horiba Scientific XploRa Raman spectrometer. The samples were investigated as received and the spectra were recorded under a microscope using a 100 × objective. The Raman-scattered light was dispersed by a holographic grating with 1200

lines mm^{-1} and detected by a CCD camera. A laser of wavelength 532 nm, filtered at 1% of its nominal power, was used. The incident power (~ 1.8 mW) was low enough to avoid any heating or damage of the samples. Each spectrum was obtained by accumulation of 2 scans from 800 to 2200 cm^{-1} over 120 s. No differences were observed among the different points of each sample and, therefore, only one spectrum was investigated in detail. Deconvolution was carried out by using five mixed Gaussian–Lorentzian profiles for the bands D_4, D_1, D_3, G and D_2 appearing at increasingly high wavenumbers [31].

Transmission electron microscopy (TEM) images were obtained with a Jeol ARM 200F (cold FEG operating at 80 kV) electron microscope.

Elemental analysis was performed with an Elementar Vario EL Cube analyser. Carbon, hydrogen, nitrogen and sulphur contents were first determined by combustion of the samples at about 1700°C (a temperature induced in a furnace, heated at 1150°C, by a tin foil wrapping the samples and used as catalyst) in a mixed stream of oxygen and helium, the latter being used as carrier gas. Oxygen was quantified with the same equipment in a second step, using a different procedure and another analytic column.

X-ray photoelectron spectroscopy (XPS) results were recorded with an ESCAPlus OMICROM system equipped with a hemispherical electron energy analyser. The spectrometer was operated at 10 kV and 15 mA, using a non-monochromatised MgKα X-Ray source ($h\nu$ = 1253.6 eV) and under vacuum (< 5×10^{-9} Torr). The hemispherical electron energy analyser operated at pass energy of 50 eV for survey spectra and at 20 eV for high-resolution spectra. The energy scale was calibrated by referencing the C1s peak to 284.5 eV. The CASA software was used for treating the XPS data.

2.4.2. Electrochemical characterisation

The electrochemical characterisation was performed with a Biologic VMP3 electrochemical workstation. The carbon electrodes were prepared by spreading a paste (~ 3 mg) containing the carbon material, polytetrafluoroethylene (PTFE) binder and carbon black in the weight percent ratio of 85:10:5 onto graphite foils (diameter 0.8 cm). The resultant electrodes were pressed at 5 MPa and impregnated with the electrolyte, 2 mol L^{-1} H_2SO_4, during 72 h.

Cyclic voltammetry (CV) tests were performed in a three-electrode cell system, using platinum gauze as the counter electrode and a saturated calomel electrode (SCE) as reference. CV curves were obtained in the potential window from 0 to 0.8 V at scan rates ranging from 0.5 to 1000 mV s^{-1}. The gravimetric capacitance of the electrode (C, F g^{-1}) was calculated from the CV curves according to Equation (2):

$$\boldsymbol{C = \frac{\int I \, \Delta t}{s \, \Delta V \, m}} \quad (2)$$

where I (A) is the current, s (V s^{-1}) is the scan rate, ΔV (V) is the potential window and m (g) is the mass of active material in the electrode.

Galvanostatic charge-discharge experiments (GCD) were studied in a two-electrode cell in the potential window between 0 and 0.8 V. Symmetrical supercapacitors were assembled by placing two identical electrodes (total mass ~ 3 mg per electrode) separated by a glass fibre disc between two gold current collectors. GCD curves were obtained at current densities ranging from 0.1 to 12 A g^{-1}, based on the total mass of the two electrodes. From these measurements, the gravimetric capacitance, C_{cell} (F g^{-1}) was calculated by applying Equation (3):

$$\boldsymbol{C_{cell} = \frac{2\,I}{m\,(dV/dt)}} \quad (3)$$

where I (A) represents the discharge current, (dV/dt) (V s^{-1}) is the slope of the discharge curve, and m (g) is the mass of active material in the electrode.

The energy density, E (Wh kg^{-1}), and the power density, P (W kg^{-1}), were calculated from GCD tests between the current densities of 0.1 and 12 A g^{-1} by applying Equations (4) and (5), respectively:

$$\boldsymbol{E} = \frac{\boldsymbol{C_{cell}}}{\boldsymbol{8\,(\Delta V - IR)^2}} \tag{4}$$

$$\boldsymbol{P} = \frac{\boldsymbol{E}}{\boldsymbol{\Delta t}} \tag{5}$$

where C_{cell} (F g^{-1}) represents the gravimetric capacitance calculated from Equation (3) and considering the mass of active material in the two electrodes, ΔV (V) is the potential difference within the discharge time Δt (s), and IR (V) is the voltage drop due to the inner resistance at the beginning of the discharge process. The cycling stability was also studied through GCD tests at the current density of 0.5 A g^{-1} up to 5000 cycles. The gravimetric capacitance for a given GCD cycle and the capacitance retention (%) were determined by using Eq. (3).

Electrochemical impedance spectroscopy (EIS) measurements were performed at open-circuit voltage in a two-electrode system within the frequency range of 100 kHz – 1 mHz, with a 10 mV alternating current amplitude. The gravimetric capacitance, C_{cell} (F g^{-1}), was calculated according to Equation (6):

$$\boldsymbol{C_{cell}} = -\frac{\boldsymbol{2\,\mathrm{Im}(Z)}}{\boldsymbol{m\,(\pi\, f\, |Z|^2)}} \tag{6}$$

where –Im(Z) (Ω) is the imaginary part of the impedance, f (Hz) is the operating frequency, $|Z|$ (Ω) is the impedance modulus, and m (g) is the active material mass for the two electrodes.

3. Results and discussion

3.1. Identification of the carbonisation steps

The thermogravimetric curves and their derivatives (TG/DTG) in argon atmosphere show what happens during the thermal decomposition between 25 and 900°C of a surfactant–tannin composite material and of tannin alone (**Figure S1-a**). The main corresponding gases evolved during the pyrolysis of the surfactant–tannin composite were detected with a mass spectrometer (**Figures S1-b**). The TG/DTG curves of mimosa tannin evidenced a continuous weight loss throughout the entire temperature range with no distinct plateau below ~800°C, indicating that thermal stability was reached only above such temperature. On the contrary, the TG/DTG curves of the surfactant–tannin composite showed that thermal decomposition occurred in three steps, mainly due to the evolution of compounds exhibiting *m*/*z* values of 18, assigned to water, and 28 and 44, which can be primarily assigned CO + CO_2 and to CO_2, respectively. The gases evolution was detected up to ~800°C. By comparing the TG/DTG curves and the mass spectrometry profiles of tannin alone and surfactant–tannin composite, it is clearly seen that most of the surfactant was removed between 284 and 404°C (44.2 % weight loss). The main products generated by surfactant decomposition were H_2O, likely originating from the condensation of the –OH terminal groups, and CO and CO_2, probably formed in reactions involving ethylene oxide and propylene oxide chains [32]. These findings suggest that the carbonisation of the surfactant–tannin composites was effective in the two steps selected herein for the OMC synthesis, i.e.: (i) a first isothermal stage, by heating the sample up to 400°C and maintaining such temperature during 4h for removing the surfactant while minimising the collapse of the phenolic matrix; and (ii) a second stage, by subsequently heating the sample up to 900°C and

maintaining this temperature for 1h in order to obtain the final carbon material. Moreover, the nitrogen isotherm data confirmed the better preservation of the mesoporosity by applying the first isothermal stage at 400°C, as shown in the textural characterisation section (see below and **Figure S2**). As for tannin alone, the thermal stability was also achieved at ~800°C, as proved by the plateau observed between 800 and 900°C and corresponding to a weight loss as low as 0.2%, associated with no further gas evolution.

3.2.Textural characterisation

The porous texture of the carbon materials was obtained from the combination of nitrogen and carbon dioxide physisorption data. The nitrogen adsorption isotherms and the corresponding pore size distributions (PSDs) of the Fi/T series of OMCs are displayed in **Figure 2** and **Figure S2** of the Supplementary Information. The effect of the carbonisation steps on the materials porosity was studied for the sample F3/30, whose nitrogen isotherms and PSDs are shown in **Figure S2** of the Supplementary Information. Charge storage in supercapacitors is a surface phenomenon, since ions are adsorbed onto the accessible pore surface of the carbon electrodes. Thus, all other parameters being equal, increasing the surface area of carbon materials may increase the specific capacitances of the resultant electrodes. The material exhibiting the highest surface area, F3/30 as discussed below, was selected to further develop its porosity through physical activation with CO_2. The nitrogen isotherms and PSDs of such activated material, C3/30, are displayed in **Figure 2**, which includes the nitrogen isotherms and PSDs of F1/10 and F3/30 for comparison. Textural parameters calculated from the nitrogen and carbon dioxide isotherms, as well as other structural parameters and carbonisation and activation yields, are gathered in **Table 1**.

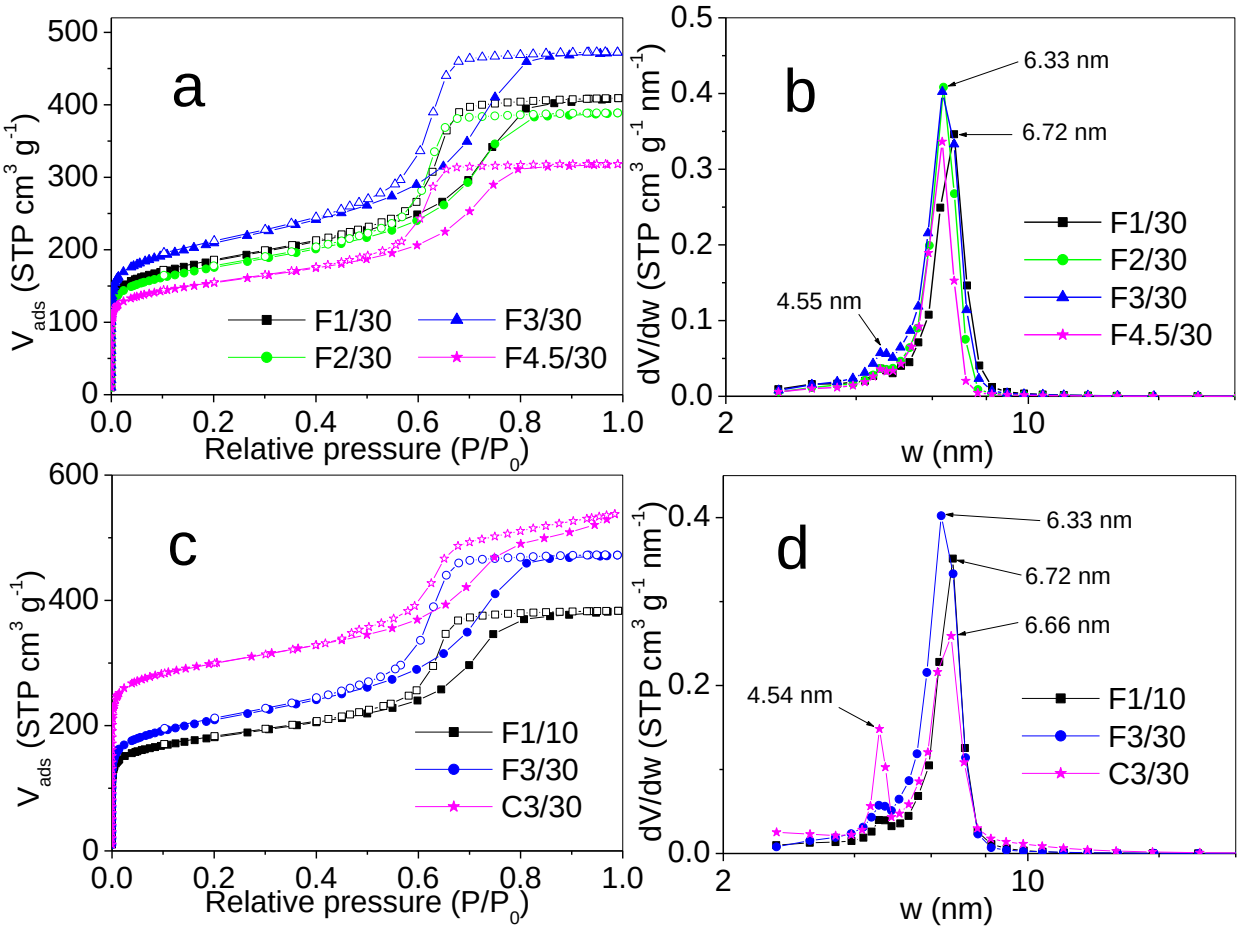

Figure 2. (a, c) Nitrogen adsorption isotherms; and (b, d) pore size distributions (PSDs) of some selected OMCs (Fi/T series) and for the activated one (C3/30).

All OMCs presented type–IV nitrogen isotherms exhibiting H2–type hysteresis loops above a relative pressure P/P_0 = 0.6, characteristic of mesoporous materials with interconnected pores and narrow PSDs [33]. Their PSDs evidenced the presence of wider mesopores with diameters of 6.28 – 7.19 nm and narrower ones of width ~ 4.55 nm (**Figure 2** and **Figure S2** in the Supplementary Information). They might be originated from the coexistence of two main diameters for those micelles or the coexistence of pores coming from micelles and gaps in the carbon walls, whose sizes mainly are 6.28 – 7.19 and ~ 4.55 nm. One-step carbonisation of the

surfactant – tannin composite material at 900°C / 3 hours (heating rate 1°C min^{-1}) yielded a different porous texture than that obtained by applying the isothermal step at 400°C / 4 h followed by carbonisation at 900 °C / 1 hour: the hysteresis loops of the isotherms became wider, the nitrogen uptake at $P/P_0 < 0.1$ decreased, and the volume of mesopores of size centred on 6.66 nm dropped significantly (**Figure S2-e** and **S2-f**). This indicates that both micropore and mesopore volumes decreased due to a partial collapse and to a poor preservation of the mesostructure during the removal of the surfactant, which was even more pronounced when the material was carbonised at 900°C / 4 hours. Thus, carbonising the materials at 400°C / 4 h for gently removing the surfactant and then at 900°C / 1 h, allowed obtaining a better preserved carbon mesostructure than in the absence of isothermal step at 400°C.

As expected, the S_{NLDFT} values were slightly higher than those of A_{BET}, given that the BET method underestimates the surface area of materials possessing narrow pores (**Table 1**) [34]. On the contrary, the DR method overestimates the micropore volumes and, due to this, the micropore volumes were calculated by applying both the DR equation ($V_{\mu\text{-}N2}$) and the Non-Local Density Functional Theory ($V_{\mu\text{-}NLDFT}$) to the nitrogen isotherms, and by applying the DR equation to the CO_2 isotherms ($V_{\mu\text{-}CO2}$) [30]. Finally, the mesopore volumes (V_M) were calculated from V_T - $V_{\mu\text{-}NLDFT}$. As shown in **Table 1**, the values of $V_{\mu\text{-}CO2}$ were lower than those of $V_{\mu\text{-}N2}$, indicating a well-developed microporosity exhibiting more supermicropores (width in the range 0.7 – 2 nm) than ultramicropores (width < 0.7 nm). It is also noteworthy that OMCs formerly obtained by hard-templating of mimosa tannin presented an important fraction of narrow pores ($V_{\mu\text{-}N2} < V_{\mu\text{-}CO2}$), which hindered ion transport and lowered the electrochemical performances under high rate and current density regimes when applied as electrode materials for supercapacitors [35]. The

effect of the porous texture on the electrochemical performances of the present materials will be discussed in the last subsection below.

Table 1. Textural parameters calculated from nitrogen and carbon dioxide adsorption isotherms, structural parameters calculated from X-ray diffraction, and carbonisation yield of the carbon materials.*

Sample	From nitrogen and carbon dioxide adsorption isotherms								From XRD		η (%)
	S_{NLDFT} ($m^2\ g^{-1}$)	A_{BET} ($m^2\ g^{-1}$)	V_T ($cm^3\ g^{-1}$)	$V_{\mu\text{-}NLDFT}$ ($cm^3\ g^{-1}$)	$V_{\mu\text{-}N2}$ ($cm^3\ g^{-1}$)	$V_{\mu\text{-}CO2}$ ($cm^3\ g^{-1}$)	V_M ($cm^3\ g^{-1}$)	t (nm)	d_{100} (nm)	a (nm)	
F1/10	758	661	0.59	0.22	0.25	0.23	0.37	6.72	13.04	15.06	27.2
F2/10	705	616	0.59	0.20	0.23	0.21	0.39	6.72-7.19	12.73	14.69	29.7
F3/10	780	691	0.63	0.23	0.26	0.23	0.40	6.72	12.73	14.69	28.6
F4.5/10	673	604	0.57	0.19	0.23	0.21	0.36	6.28-6.72	12.43	14.35	29.0
F1/20	788	664	0.60	0.23	0.25	0.24	0.37	7.14	14.47	16.71	27.0
F2/20	715	614	0.59	0.21	0.23	0.22	0.38	7.17	13.72	15.84	28.0
F3/20	786	691	0.63	0.23	0.26	0.23	0.40	6.75	12.73	14.69	26.5
F4.5/20	668	601	0.58	0.19	0.23	0.21	0.39	6.31-6.75	13.37	15.44	28.0
F1/30	744	667	0.63	0.22	0.25	0.23	0.41	6.72	13.04	15.06	27.2
F2/30	705	634	0.60	0.20	0.24	0.22	0.40	6.33	12.14	14.02	28.2
F3/30	827	750	0.73	0.24	0.28	0.26	0.49	6.33	11.87	13.71	26.8
F4.5/30	583	563	0.49	0.17	0.21	0.19	0.32	6.33	14.08	16.26	26.9
C3/30	1152	1137	0.83	0.38	0.44	0.34	0.45	6.66	11.93	13.77	18.9

* S_{NLDFT}: calculated by applying the NLDFT method to CO_2 and N_2 adsorption isotherms; S_{BET}: calculated by applying the BET equation to the nitrogen adsorption isotherms; V_T: total pore volume; $V_{\mu\text{-}NLDFT}$: micropore volume calculated by applying the NLDFT method to CO_2 and N_2 adsorption isotherms; $V_{\mu\text{-}N2}$: micropore volume calculated by applying the Dubinin – Radushkevich (DR) equation to the nitrogen adsorption isotherms; $V_{\mu\text{-}CO2}$: ultramicropore volume determined by applying the Dubinin-Radushkevich (DR) equation to the carbon dioxide isotherms; V_M: mesopore volume, calculated as the difference V_T - $V_{\mu\text{-}NLDFT}$; t: thickness of the carbon walls, calculated as the difference $a - w$, where a is the unit cell parameter and w is main pore size of the BJH-KJS distributions; d_{100}: interplanar spacing; a: unit cell parameter, calculated as $(2/\sqrt{3})\times d_{100}$; η: carbonisation yield for the Fi/T series and (carbonization + activation) yield for the activated OMC.

For a given temperature, increasing the pH from 1 to 4.5 did not produce, on average, significant changes in the porosity of the carbons. Among the non-activated materials, the most remarkable differences were found for those synthesised at pH 3, which exhibited the highest A_{BET} and pore volumes, irrespective to the temperature of self-assembly used to prepare them. For a given pH value, an increase of the assembly temperature from 10 to 20°C did not lead to significant changes in the carbon porosity, as only a slight widening of the PSD was observed for F1/20 and F2/20 (**Figure S2** in the Supplementary Information). However, increasing the assembly temperature from 20 to 30°C produced an increase of micropore volume and a little increase of mesopore volume, especially for the samples synthesised at pH 3. In fact, among all studied carbons, F3/30 presented the highest values of both A_{BET} and V_T, 750 m^2 g^{-1} and 0.74 cm^3 g^{-1}, respectively. This sample not only exhibited the highest micropore volume, 0.24 cm^3 g^{-1}, but also the highest mesopore volume, 0.49 cm^3 g^{-1} (see again **Table 1**). F3/30 also possessed the highest volume of mesopores with diameters centred on 6.66 nm and a narrow PSD in the mesopore range. This suggests that F3/30 exhibits the most ordered mesoporous structure among the studied carbons, which assumption will be confirmed by XRD. These observations can be explained by flavonoid units autocondensing at different extents, depending on pH and temperature: (i) autocondensation of tannin occurs preferably at pH < 3 than at pH = 3: –OH groups of flavonoids condensate with each other so that H_2O is released to the aqueous solution, and lead to more compact structures [36–39]; (ii) as tannin autocondensation is an exothermic process, increasing temperatures from 10 to 30°C hinder this reaction by thermodynamic reasons ($\Delta H < 0$) [38–40]; this could make the polymer network less compact and –OH groups could be released from the material during pyrolysis as H_2O molecules, thus generating further pores (**Table 1**).

The carbonisation yield of the Fi/T series was 28.1 ± 1.6 %. The activated carbon, C3/30, exhibited an activation yield of 70.4% and a (carbonisation + activation) yield of 18.9%. C3/30 exhibited micropore and mesopore volumes of 0.38 and 0.45 $cm^3\ g^{-1}$, respectively, and a BET surface area of 1137 $m^2\ g^{-1}$ (**Table 1**). Therefore, physical activation allowed increasing the micropore volume by 58.3% compared to F3/30, but the mesopore volume decreased by 8.2% and the PSD was modified in the mesopore range: the volume of mesopores with diameters centred on 6.33 nm decreased and was shifted towards slightly higher diameters of 6.66 nm, the volume of mesopores of sizes higher than 9 nm increased and that of mesopores with diameters of 4.54 nm increased; as the size of the latter did not change during activation but only their volume increased, it seems that these pores were pre-existing and that activation made them more available. The volume of narrow micropores in C3/30, 0.34 $cm^3\ g^{-1}$, increased compared to that of the non-activated F3/30, 0.26 $cm^3\ g^{-1}$. The changes of porous texture of C3/30 with respect to F3/30 thus agree with what was expected for a physical activation, being non-selective carbon gasification for generating porosity and widening the pre-existing pores.

3.3.Structural and nanotextural characterisation

The structural order at the mesoscale of the obtained carbons was studied by small–angle XRD in the range of 2θ Bragg angles from 0.5 to 4° (**Figure 3a**). The XRD profiles presented one band centred on 2θ = 0.68 ± 0.07°, which is associated with the (100) reflection of the 2D–hexagonal P6mm spatial group [24,33]. However, the absence of bands corresponding to the (110) and (200) reflections of the same spatial group indicates that these materials are not ordered at long range [33]. No clear trends were observed in the d_{100} or a values of the carbons synthesised at increasing pH but fixed self-assembly temperature. F3/30 exhibited the XRD

profile with the most intense and narrow (100) band, suggesting, together with the results of textural properties, that this material possesses the most ordered structure. The d_{100} values were in the range of 11.87–14.47 nm for F3/30 and F1/20, respectively, and the corresponding a values calculated from **Equation 1** were in the range of 13.71 – 14.47 nm, respectively. Physical activation did not change significantly the d_{100} and a values of C3/30 with respect to those of F3/30, which means that the structural order was maintained. It is noteworthy that both parameters d_{100} and a are higher than those obtained for formerly studied tannin-derived OMCs [28]; this means that our materials underwent lower structural shrinkage during carbonisation. In fact, both parameters are similar to those obtained for soft-templated carbons prepared from resorcinol-formaldehyde resins, which are thermosetting polymers exhibiting low structural shrinkage when carbonised [32]. In the two aforementioned works, highly acidic conditions were used to obtain OMCs. Thus, interestingly, the structural shrinkage of the present tannin-derived OMCs was not only lowered by controlling the temperature of both self-assembly and carbonisation steps, but the materials were prepared under milder pH conditions than those reported before, and in the absence of formaldehyde or toxic phenolic molecules.

TEM images of some representative OMC samples confirmed that the latter possess 2D–hexagonal ordered structures, regardless of pH or self-assembly temperature used to prepare them (**Figure 3b** and **Figure S3** in the Supplementary Information). Considering the scheme of the soft–templating method displayed in **Figure 1**, the empty spaces observed in the TEM images (in white) correspond to the pores created by removing the surfactant, while the black parts correspond to the carbon derived from tannin. TEM images along the longitudinal direction of the ordered structures show that the pores are organised in linear arrays at regular intervals and present an average diameter of ~ 6.5 nm (mesopores). The presence of some gaps inside the

carbon walls is related to the lower structural order along the (110) and (200) directions, as observed by small-angle XRD. Taken into account the textural results exposed above, this is in agreement with the coexistence of pores coming from surfactant micelles and gaps in the carbon walls, 6.28 – 7.19 and ~ 4.55 nm in size.

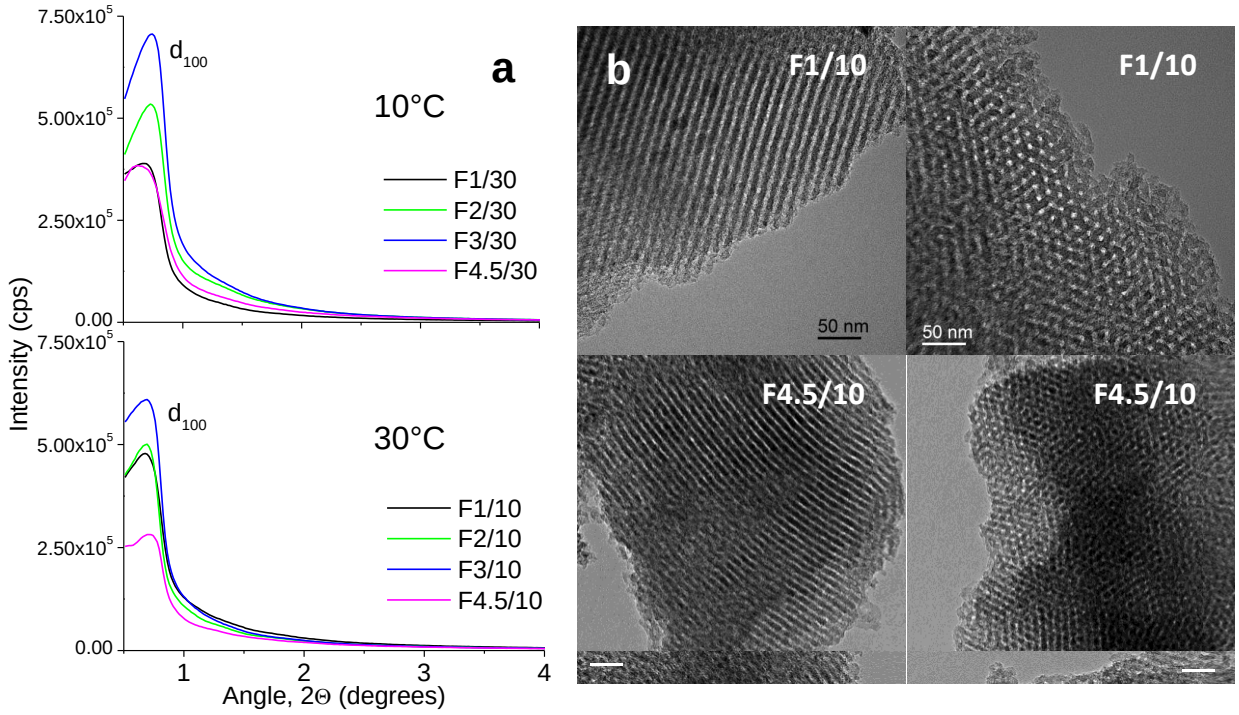

Figure 3. (a) Small–angle XRD profiles of the soft-templated OMCs prepared at the self-assembly temperatures of 10°C (top) and 30°C (bottom); (b) TEM images of F1/10 and F4/10 in the longitudinal direction (left raw) and in the cross-sectional direction (right raw).

The first–order Raman spectra of the OMCs synthesised at different values of temperature and pH are displayed in **Figure S4** in the Supplementary Information. The $I(D_1) / I(G)$ ratios of the OMCs at different pH and assembly temperatures are shown in **Figure 4**. All the materials presented broad D_1 and G bands of rather similar intensity, typical of disordered carbon materials [41,42]. On the one hand, the materials prepared at 10°C and pH values from 1 and 4.5 exhibited

D_1 and G bands located at 1342 ± 1 and 1592 ± 2 cm^{-1}, respectively. On the other hand, those prepared at pH 1 and at self-assembly temperatures between 10 and 30°C displayed D_1 and G bands located at slightly higher Raman shifts, 1343 and 1595 cm^{-1}, respectively (**Figure S4** in the Supplementary Information).

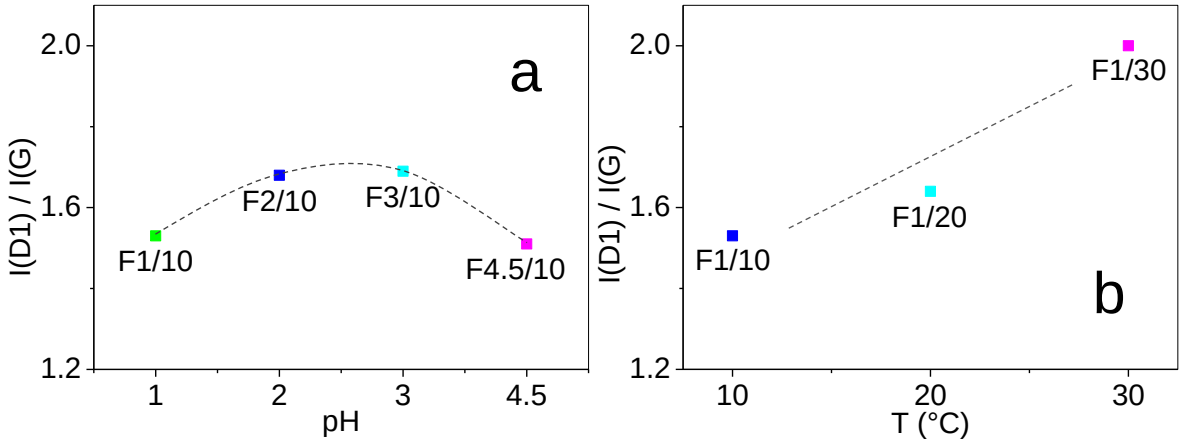

Figure 4. Intensity ratio of D to G bands, *I(D)* / *I(G)*, obtained from the first-order Raman spectra of the studied OMCs as a function of: (a) synthesis pH; and (b) assembly temperature.

The comparable intensities of the D_1 and G bands are only apparent, as the envelopes of the spectra can be accounted for by three more components (D_4, D_3 and D_2) appearing between 1210 and 1602 cm^{-1}, respectively (**Figure S4** in Supporting Information section). D_4 is responsible for the left shoulder of the spectra and is related to the poor organization of carbon. D_2 is responsible for the right shoulder of the spectra and corresponds to the second first-order zone boundary phonon. D_3 is required for filling the gap between D_1 and G bands and appears when the crystallization degree is very low. The width of D_1 is related to both the crystallite size (L_a) and the contribution of edge planes, while the width of the G peak is proportional to the disorder produced at sp^2 sites because of the presence of sp^3 carbon [43].

The studied carbons are non-graphitic materials since they do not possess 3D long–range graphitic structure, and are also non-graphitisable since the turbostratic units are randomly arranged and bridged to each other by disordered carbon species, even after carbonisation at temperatures as high as 2000°C [44]. Accordingly to this, the $I(D_1) / I(G)$ ratios are expected to be proportional to the squared crystallite size, L_a^2 [42]. The $I(D_1) / I(G)$ ratios moderately increased in the range of pH from 1 to 3 and decreased at pH 4.5, while they exhibited a clear increasing trend as the self-assembly temperature increased from 10 to 30 °C. This suggests that the crystallite size increased in the range of pH 1 to 3 and at increasing temperatures, thus improving the nano-textural order of the corresponding materials, and decreased at pH 4. This finding indicates an improvement of the assembly of tannin with surfactant in the mentioned pH (1 to 3) and temperature conditions, and agrees with the progressively increasing mesostructural order of the materials as the pH increased from 1 to 3. On the other hand, this trend is different to that of a previous work also dealing with the synthesis of OMCs from mimosa tannin and Pluronic® F127, in which an increase of the nanotexture order was observed as the medium pH decreased from 4.2 to 0 [28]. Given that no control of the tannin–surfactant assembly conditions (time and temperature) was exerted in the latter work, it seems that both parameters play a key role on the nanotexture order of the resultant OMCs and allow using milder pH conditions.

The different porous textures and nano-textural and structural orders of the studied OMCs as a function of pH can be explained in terms of the self-assembly mechanism followed by triblock copolymer and tannin molecules. Different pathways have been used to describe the synthesis of ordered mesoporous materials under different pH conditions [2]. In the case of OMCs prepared from resorcinol-formaldehyde resins and triblock copolymer surfactants in highly acidic media, the organic-organic self-assembly is mediated by $I^+X^-S^+$ and hydrogen-bonding (I^0S^0)

interactions [32], where I^+ and S^+ refer to the protonated groups of the precursor and the hydrophilic blocks of the triblock-copolymer, respectively, and X^- refers to counter ions (e.g. Cl^-). Under highly acidic conditions, for example in HCl medium, the -OH groups of the molecules of carbon precursor and the hydrophilic blocks of the triblock copolymers are protonated, and the Cl^- ions act as mediators (X^-); the Coulombic interactions existing among them can facilitate the $I^+X^-S^+$ pathway and enable the self-assembly of the surfactant-polymer nanocomposites. On the one hand, the assembly of tannin with triblock copolymers is expected to be governed by both the $I^+X^-S^+$ and I^0S^0 mechanisms, since tannins are polyphenols that are able to lead to the same kinds of reactions as phenol or resorcinol [45]. On the other hand, tannin molecules are also prone to autocondensation under highly acidic conditions and give rise to highly disordered carbon after pyrolysis [36–39]. **Figure 5** thus illustrates the formation of tannin aggregates (in dark brown colour) produced by tannin autocondensation at pH 1, and which is hindered when the pH increases. Thus, as the pH of the medium increased from 1 to 3, the long-term order at the mesoscale, the volume of mesopores with diameters centred on 6.72–7.19 nm and the nanotexture order, increased due to a progressive hindrance of tannin autocondensation, which is in competition with the formation of the ordered mesostructure through well-organised self-assembly. The maximum textural order at the mesoscale was found for the samples synthesised at pH 3, illustrating that the supramolecular structure is better stabilised through stronger interactions than at lower pH values, the latter favouring autocondensation. However, when no HCl was added to the tannin solution (pH 4.5), the absence of H^+ and Cl^- ions involved in the –OH group protonation and in the formation of the ordered template, mediating the tannin-surfactant interactions through the $I^+X^-S^+$ and I^0S^0 mechanisms, produced a decrease of both long-term structural order and mesopore volume [2,28]. pH 3 thus appear to be an optimum.

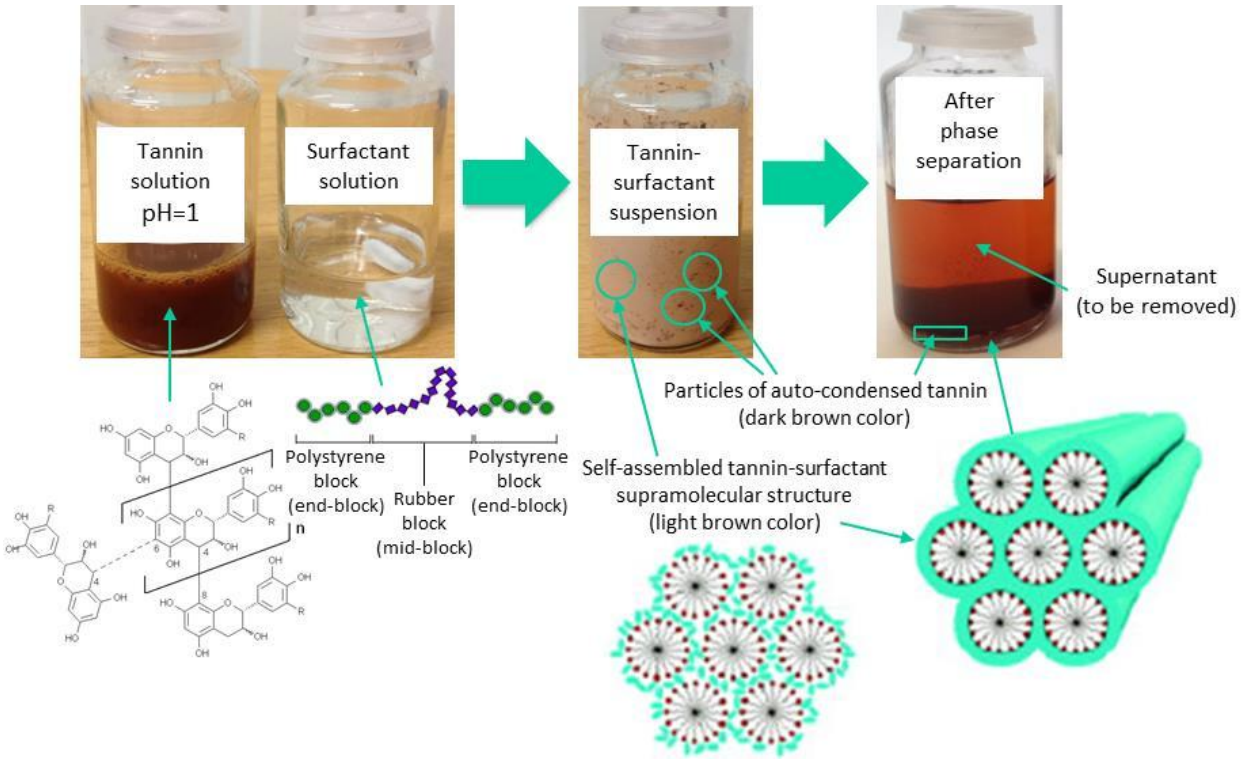

Figure 5. Competitive formation of tannin-surfactant supramolecular structures by self-assembly, and of tannin aggregates by autocondensation of tannin at pH 1.

3.4. Chemical characterisation

Table S1 of the Supplementary Information collects the results of bulk chemical composition of the studied OMCs, Fi/T series and C3/30, expressed as wt. % and at. %. The Fi/T materials exhibited low nitrogen concentrations, between 0.06 and 0.15 wt. % (0.04 and 0.12 at. %), due to a few amino acids leached with tannin from mimosa barks during the extraction process. These values are so low that the materials cannot be considered nitrogen-doped. Physical activation of F3/30 into C3/30 increased the bulk carbon content and decreased the bulk concentration of the other elements, which suggests the release of functional groups located at the edges of carbon layers. Thus, the carbon content increased by 1.2% and the oxygen content,

for example, decreased by 12.8%. Interestingly, as the assembly temperature increased from 10 to 30°C, the oxygen content decreased: the samples synthesised at 10°C possessed the highest oxygen concentrations, up to 6.59 wt. % for F3/10 (4.27 at. %), while those synthesised at 30°C presented the lowest ones, not higher than 4.27 wt. % for F4.5/30 (3.05 at. %).

This trend is clearly seen in the 3D–Van Krevelen diagram given in **Figure 6**, which shows the N/C, O/C and H/C atomic ratios of the studied materials. It agrees with a lower autocondensation of tannin molecules as the assembly temperature increases at a given pH: the less compact polymer network produced at higher temperature of synthesis allows the release of more –OH groups during carbonisation, leading to higher pore volumes and surface areas as shown above but also to lower bulk O concentrations in the final carbons.

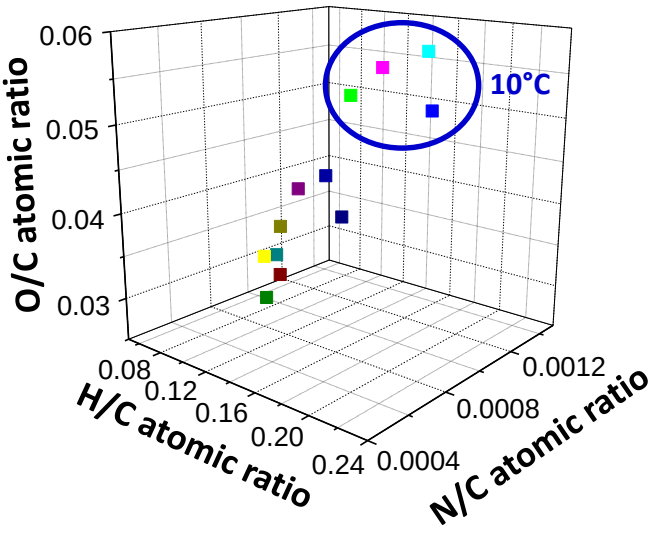

Figure 6. Van Krevelen diagram of the studied OMCs.

The chemical composition of the materials' surface was studied by XPS, and the resulting data, expressed as at. %, are collected in **Table 2**. The C1s and O1s high-resolution spectra for some representative Fi/T materials, as well as for C3/30, are displayed in **Figures S5**, **S6** and **S7**

of the Supplementary Information. As shown in **Table 2**, no nitrogen was found at the materials surface because of its well-known volatility during carbonisation. In agreement with the results of elemental analysis, the surface concentration of oxygen was found to be higher for samples synthesised at 10°C than for those prepared at 20 and 30°C, and F3/10 exhibited the highest oxygen surface concentration of 3.5 at. %. The oxygen surface concentrations of the samples prepared at 10°C (**Table 2**) were lower than in the bulk (see in at. % values in **Table S1**), indicating that the oxygen functionalities were mainly located in the materials bulk. However, the oxygen surface concentrations of the materials prepared at 20 and 30°C were similar or slightly higher than those found in the bulk, indicating a more homogeneous distribution of the oxygen groups all through the materials. As for the elemental analysis results, such differences can also be explained in terms of different autocondensation degree as a function of the assembly temperature: at 20 and 30°C, tannin autocondensation occurs to a lower extent than at 10°C so that less compact polymer networks are formed, in which the many hydroxyl groups are more equally distributed all through the material and out of which the latter can be more easily and more homogeneously released as water during carbonisation. Such less reticulated polymers and easier release of water molecules is consistent with the higher micropore volume of OMCs prepared at higher assembly temperatures, as already explained in the textural characterisation section. Physical activation increased the carbon content and reduced the nitrogen and oxygen contents, both in the bulk and at the surface of C3/30. This is also consistent with the removal of functional groups located at the edges of carbon layers by CO_2 activation. Oxygen was homogeneously distributed, as the oxygen content of the material was 2.0 and 2.1 at. % in the bulk and at the surface, respectively.

Table 2. Surface composition obtained by XPS and contributions to the C1s and O1s peaks.*

Sample	XPS		C1s					O1s		
	C (at. %)	O (at. %)	CI BE (eV) A (%)	CII BE (eV) A (%)	CIII BE (eV) A (%)	CIV BE (eV) A (%)	CV BE (eV) A (%)	OI BE (eV) A (%)	OII BE (eV) A (%)	OIII BE (eV) A (%)
F1/10	96.9	3.1	284.5 (65.7)	285.5 (24.4)	287.6 (6.2)	289.0 (0.2)	290.1 (2.8)	531.7 (35.1)	532.9 (55.7)	534.5 (9.2)
F2/10	96.6	3.4	284.5 (65.1)	285.5 (25.0)	287.6 (7.0)	289.2 (1.0)	290.3 (2.0)	531.6 (32.6)	532.9 (58.7)	534.5 (8.8)
F3/10	96.5	3.5	284.5 (66.7)	285.5 (23.0)	287.6 (6.8)	289.1 (0.5)	290.2 (2.9)	531.6 (37.5)	532.9 (53.9)	534.5 (8.6)
F4.5/10	96.9	3.1	284.5 (67.0)	285.5 (23.3)	287.6 (7.0)	289.1 (0.5)	290.2 (2.4)	531.6 (34.1)	532.9 (58.4)	534.5 (7.6)
F1/20	97.1	2.9	284.5 (65.1)	285.5 (25.4)	287.6 (6.5)	289.0 (0.5)	290.2 (2.8)	531.8 (35.6)	533.0 (53.8)	534.5 (10.6)
F4.5/20	96.7	3.3	284.5 (66.2)	285.5 (23.8)	287.6 (7.0)	289.1 (0.6)	290.3 (2.3)	531.7 (35.6)	532.9 (57.5)	534.5 (6.9)
F1/30	97.5	2.5	284.5 (67.6)	285.5 (22.7)	287.6 (6.9)	289.2 (0.8)	290.3 (2.3)	531.8 (39.4)	533.0 (54.4)	534.5 (6.2)
F4.5/30	96.8	3.2	284.5 (66.0)	285.5 (24.4)	287.6 (6.9)	289.1 (0.5)	290.2 (2.1)	531.7 (34.0)	532.9 (56.4)	534.5 (9.6)
C3/30	97.9	2.1	284.5 (72.6)	285.5 (23.2)	287.6 (2.7)	289.2 (0.2)	290.1 (1.2)	531.2 (28.6)	532.6 (63.6)	534.5 (7.8)

*Assignment of the peaks: CI are hydrocarbons, aromatics and aliphatics; CII are Csp^3 and C-O single bonds associated with ethers, phenols and anhydrides; CIII are C=O double bonds in carbonyls and quinones; CIV are C-O single bonds in carboxyls; CV are plasmon losses or shake-up π-π satellites. OI are C=O double bonds in quinone-type groups, carbonyls and carboxylic acids; OII are –OH bonds in phenols, C–O–C ether groups and C=O bonds in ester and anhydride groups; OIII are chemisorbed oxygen, single C-O bonds in esters and anhydrides, C-O bonds in carboxylic groups and/or water [46–48]. BE and A (%) stand for binding energy and relative contribution based on peak area, respectively.

Deconvolution of the C1s and O1s high-resolution spectra allowed identifying a variety of oxygen functionalities at the materials surface (**Figures S5, S6** and **S7** of the Supplementary Information, and **Table 2**). No significant differences were found among the binding energies and relative areas of each type of contribution for the different OMCs, which suggests that their

surface chemistries were similar after carbonisation. Phenols, ethers, esters and anhydrides were the most abundant oxygen functionalities, followed by carbonyls, quinones and carboxylic acids (**Table 2**). Among those oxygen functionalities, mainly quinones and carbonyl groups but also hydroxyl and carboxylic groups have been proved to be electrochemically active in protonic acidic electrolytes, such as sulphuric acid (see possible reactions in **Figure S8** of the Supplementary Information**)**. Removal of oxygen groups from the C3/30 surface during activation of F3/30 was evidenced by: (i) the increase of the relative amounts of hydrocarbons, aromatics and aliphatics (peak CI), and (ii) the decrease of the relative amounts of carbonyls, quinones and carboxylic acids (peaks CIII, CIV, CV, OI and OIII). The increase of relative area of the OII peak could indicate an increase in the relative concentration of phenols, ethers, esters and anhydrides. But, as OIII peak is also related to the presence of ester and anhydride groups, and given that the OIII relative area decreased, no clear conclusions can be drawn for the ester and anhydride evolution..

4. Electrochemical performances

Electrochemical properties of the carbon-based electrodes were studied by cyclic voltammetry (CV) in a three–electrode cell, and by galvanostatic charge–discharge (GCD) and impedance spectroscopy (EIS) in a two–electrode cell. Electrochemical tests were carried out at room temperature using 2 mol L^{-1} H_2SO_4 as aqueous electrolyte, and the obtained results are displayed in **Figures 7** and **8**, as well as in **Figure S9** of the Supplementary Information.

Cyclic voltammograms were recorded at different scan rates between 0.5 mV s^{-1} and 1 V s^{-1} in the potential range of 0 – 0.8 V. At the lowest scan rate, 0.5 mV s^{-1}, the CV curves exhibited quasi-rectangular profiles with small redox peaks, suggesting the contribution of reversible redox

reactions of oxygen groups to the total capacitance of the electrode (**Figure 7a**). F1/10 and F3/30 electrodes exhibited gravimetric capacitances of 158 and 193 F g^{-1}, respectively, while that based on C3/30 reached 286 F g^{-1} (**Figure 7b**). This illustrates that activation of F3/30 increased the gravimetric capacitance by 1.5 times. The volumetric capacitances of the electrodes were 96, 119 and 158 F cm^{-3} for F1/10, F3/30 and C3/30, respectively. OMCs formerly reported, obtained by soft-templating of resorcinol / phloroglucinol – formaldehyde resins with Pluronic® F127 and subsequently submitted to HNO_3 oxidation, exhibited lower specific capacitances up to 270 F g^{-1}, measured in a three-electrode cell using 1 mol L^{-1} H_2SO_4 electrolyte [49]. In contrast, the present OMCs are not only based on natural precursors in the absence of toxic agents such as resorcinol and formaldehyde, but no oxidation post-treatment generating polluting washing liquids had to be used. The redox peaks of the CV curves no longer appeared above 10 mV s^{-1}, indicating that charge storage mainly occurred through a capacitive mechanism. As the scan rate increased from 0.5 mV s^{-1} to 1 V s^{-1}, the specific capacitance gradually decreased, which can be explained by the progressive resistance increase to ion diffusion into the carbon pores at increasing scan rates. At the very high scan rate of 1 V s^{-1}, the materials yielded similar capacitance retentions of 13 ± 1 % (**Figure S9-a** in Supporting Information). Interfacial capacitances of the electrodes at different scan rates, C / A_{BET}, were plotted versus oxygen surface concentrations in order to determine the pseudocapacitance contribution to the overall capacitance (**Figure 7c**). Increasing the surface oxygen concentration had not effect on the interfacial capacitances, even at the lowest scan rate of 0.5 mV s^{-1}. This fact suggests that charge is mainly stored through an electric double layer mechanism in which the porous texture is the key parameter, and that the pseudocapacitance contribution was negligible.

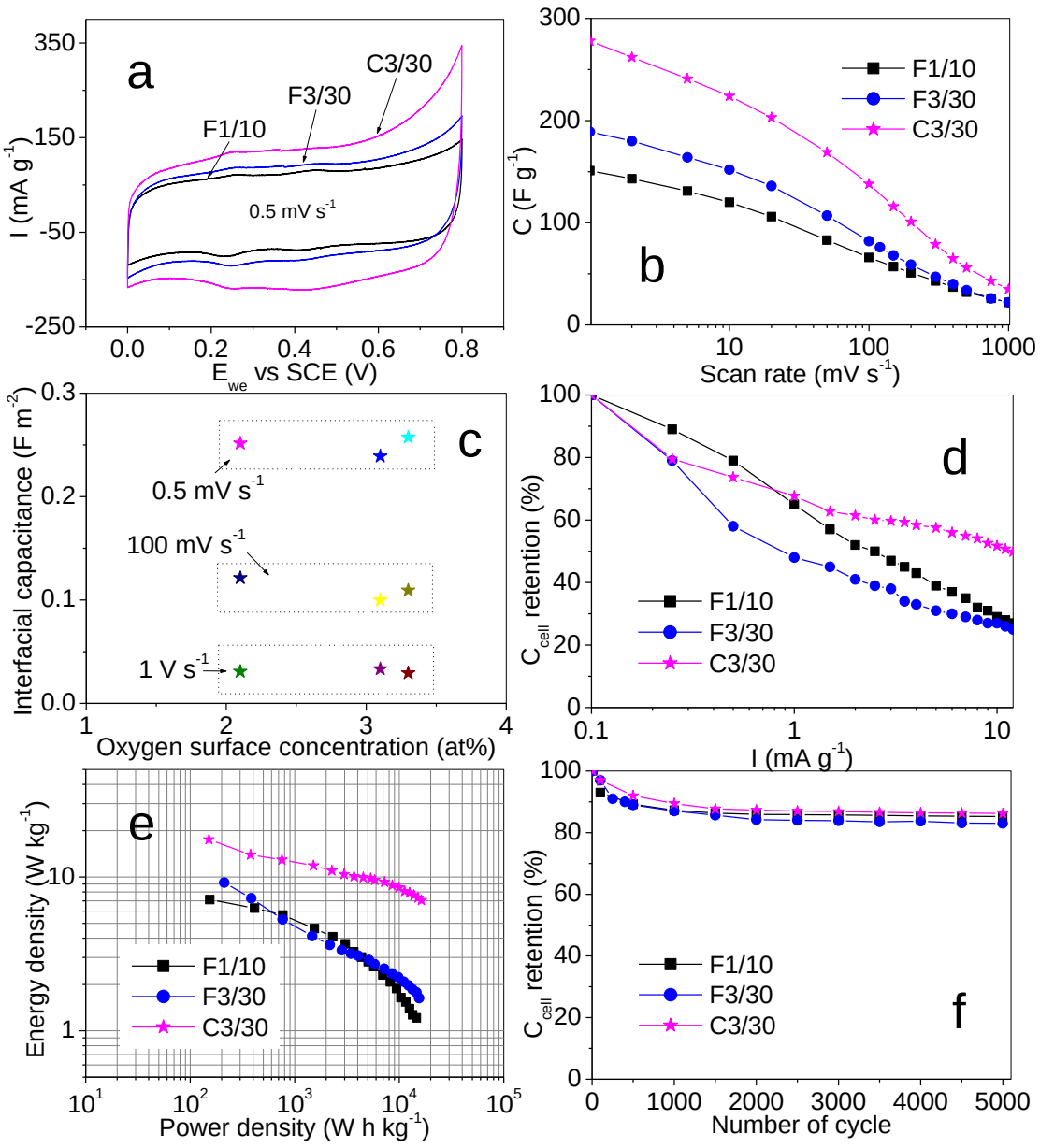

Figure 7. CV results obtained in a three–electrode cell for the studied materials: (a) CV curves at 0.5 mV s^{-1} scan rate in the potential window of 0 – 0.8 V; (b) changes of gravimetric capacitance with scan rate; and (c) interfacial capacitance vs atomic surface concentration of oxygen, obtained by XPS, at different can rates. Electrochemical performances of the two–electrode system: (d) percentage of capacitance retention as a function of current density, determined by GCD; (e) Ragone plot; and (f) cycling stability up to 5000 cycles of charge–discharge.

GCD tests were carried out at different current densities between 0.1 and 12 A g^{-1} in the voltage range of 0 – 0.8 V. The GCD curves of the carbon electrodes exhibited quasi-triangle shaped curves up to the high current density of 12 A g^{-1} and increasing Ohmic drops (IR drops), indicating that charge propagation was progressively less reversible with increasing current densities. GCD curves of the carbon electrodes obtained at 4 A g^{-1} current density are shown as representative examples in **Figure S9-b** in the Supplementary Information. Typically, the GCD curves of carbon electrodes exhibit ohmic drops (IR drops) that are attributed to the electrolyte resistance (R_s) and the inner resistance for ion migration in micropores (R_i) [50]. At the high current density of 4 A g^{-1}, for example, F3/30 exhibited the highest IR drop of 0.0577 V while C3/30 exhibited the lowest one, 0.0273 V (**Figure S9-b**). The inner resistance of ion migration has a higher contribution to the whole IR drop and is one of the intrinsic characteristics of the carbon electrodes [50]. Thus, the measured potential drop in the discharge curve should be proportional to the discharge current, and the slope of the linear relationship would be an estimation of the inner resistance (R_i) of the electrodes [51]. The variation of the IR drop with the discharge current for the studied electrodes is represented in **Figure S9-c** of Supporting Information. Interestingly, C3/30 exhibited the lower internal resistance than F3/30, 2.70 and 5.30 Ohms, respectively, despite possessing a much higher micropore volume. The lower resistance for ion migration of the C3/30 electrode could be explained by the decrease of the oxygen surface concentration upon activation and to the widening of the pre-existing micro and mesopores, as already proven for activated carbons obtained at progressively higher activation times [51,52].

The capacitance values obtained through GCD in the two-electrode cell (two carbon electrodes in series) can be compared with those obtained through CV in a three-electrode cell

(one carbon electrode) by expressing them as the capacitance of a single carbon electrode, through the equation $C_{electrode} = 4\ C_{cell}$ [53]. Thus, C3/30 yielded the highest specific capacitance of 244 F g^{-1} at 0.1 A g^{-1}, expressed for a single electrode. Interestingly, the specific capacitance of C3/30 is higher to that of other activated carbons obtained by CO_2 activation of phenolic resins, 199 F g^{-1}, despite the latter possessed micro-mesoporous hierarchical structures as well as surface areas as high as 1488 m^2 g^{-1} [54]. Moreover, GCD of such activated carbons was carried out in a three-electrode cell at a lower current density of 0.05 A g^{-1}; thus, the reported specific capacitances would be even lower under the same experimental conditions of in our work, as it is well-known that two-electrode cell and higher current densities give rise to lower capacitance values.

The specific capacitances progressively decreased from 0.1 to 12 A g^{-1} for the studied materials, due to the increasing both electrolyte resistance and inner resistance to ion diffusion: F1/10 and F3/30 exhibited lower capacitance retentions of 26 ± 1%, while 50% of the initial capacitance was still retained for C3/30 at the very high current density of 12 A g^{-1} (**Figure 7d**). The higher specific capacitance retention is explained by the increase of the micropore volume and the presence of mesopores and inter-connected pore channels in the activated OMC. It is generally accepted that, during the charge–discharge process, micropores account for ion storage while mesopores facilitate the diffusion of electrolyte ions towards micropores. Thus, hierarchical porous structures comprising balanced micropore and mesopore volumes are generally associated with higher electrochemical performances at both high scan rates and current densities.

Symmetrical supercapacitors made from F1/10 and F3/30 delivered maxima energy densities of 7.13 and 9.20 Wh kg^{-1}, respectively, and maxima power densities of 14.56 and 15.46 kW

kg^{-1}, respectively (**Figure 7e**). The C3/30 supercapacitor led to exceptionally high energy and power densities of 17.54 W kg^{-1} and 16.29 kW kg^{-1}, respectively, in a range of current densities from 0.1 to 12 A g^{-1}. These values are higher than those obtained for other carbon materials with hierarchical porosities in 2 mol L^{-1} H_2SO_4 electrolyte (maxima energy densities of 4.5 Wh kg^{-1} and power densities of ~ 3 kW kg^{-1}) [54], and can be primarily assigned to the high micropore and mesopore volumes as well as to the ordered structure of the OMCs.

Long-term cycling stability of the carbon electrodes was tested at 0.5 A g^{-1} current density up to 5000 cycles of charge-discharge, and the corresponding results are displayed in **Figure 7f**. The capacitance retention slightly decreased until 1000 charge-discharge cycles, and 84.6 ± 1.6% of the specific capacitance was retained after 5000 cycles. C3/30 yielded the best long-term stability, since the capacitance retention reached the highest value of 86.2%. Such an excellent stability may be related to both the hierarchical porous texture of the material, comprising high micropore and mesopore volumes, and the low concentration of oxygen functionalities, which have been proven to increase ESR and deteriorate capacitance, thus contributing to capacitor instability [51,53,55].

Electrochemical impedance spectroscopy (EIS) was further used to study the frequency response of the materials in the symmetric two−electrode system (**Figure 8**). Nyquist plots are typical of porous materials and exhibit three distinct zones (**Figure 8a**): (i) semicircles in the high-frequency region, (ii) straight lines tilted at 45° in the intermediate frequency region, and (iii) straight lines of higher slope in the low-frequency region. Semicircles are related to electron transfer resistance at the electrode-electrolyte interface, whereas the 45°-tilted straight lines are associated with Warburg impedance, which gives information about ion diffusion resistance into the carbon electrode. Both electron transfer resistance and ion diffusion resistance contribute to

the impedance of the system, which is affected by the density of oxygen surface groups and by the shape and the diameter of the pores. F3/30 exhibited the semicircle of highest diameter, 0.82 Ω, while C3/30 exhibited the smallest one, 0.57 Ω, indicating that electron transfer resistance decreased after activation. Moreover, the length of the Warburg segment of C3/30 was lower than that of F3/30, indicating a decreased resistance to ion transport into the electrode bulk, in agreement with the GCD results. As commented above, the decrease of both the electron transfer resistance and the diffusion resistance can be likely due to the decrease of the oxygen groups concentration and to the widening of the pre-existing micro and mesopores upon activation [52].

The equivalent series resistance (ESR) of the system was calculated from the intercept of the linear region at low frequency with the axis of the real part of the impedance. The ESR comprises electrolyte resistance, intrinsic resistance of the active material, and interfacial contact resistance between the active material and the current collector [15]. C3/30 exhibited the highest ESR, 4.80 Ω, suggesting that this material presents the lowest electrical conductivity, which is in agreement with the porosity generation by activation. The gravimetric capacitances, calculated at 1 mHz for the two-electrode systems, were 45, 36 and 28 F g^{-1} for C3/30, F3/30 and F1/10, respectively. The gravimetric capacitances of a single electrode, calculated through the above equation $C_{electrode} = 4\ C_{cell}$, were 180, 144 and 112 F g^{-1} for C3/30, F3/30 and F1/10, respectively. As expected, they are lower than those capacitance values determined by CV and GCD, since they were determined through different techniques, but they keep the same trend for the three carbons (capacitance values in the order: C3/30 > F3/30 > F1/10).

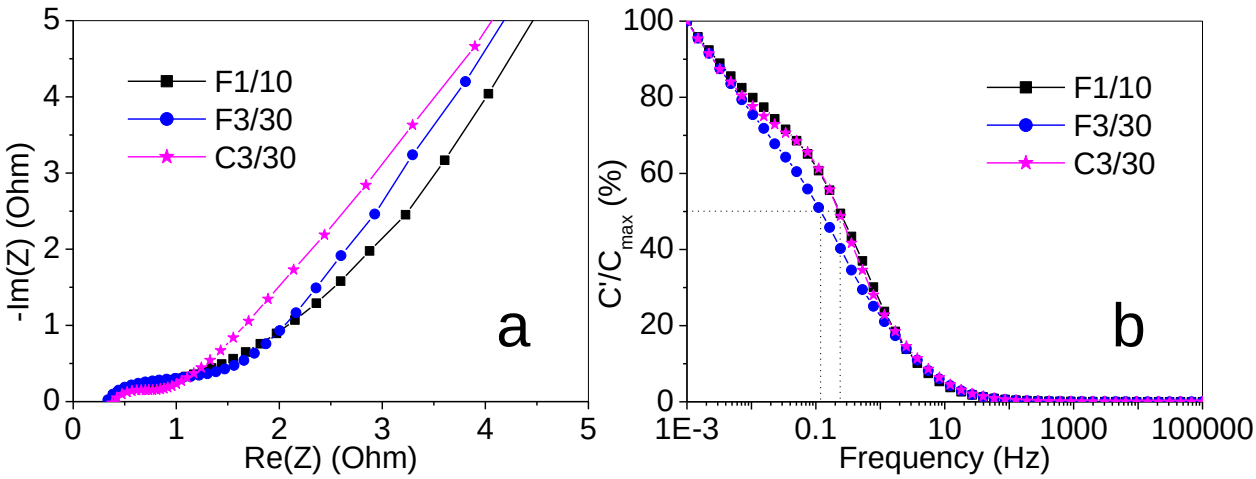

Figure 8. EIS results obtained in a two–electrode cell: (a) Nyquist plot; and (b) frequency response plot.

The frequency dependence of the capacitance was studied by EIS in a two-electrode system. **Figure 8b** shows the evolution of the normalised capacitance, C'/C_{max}, or the real component of capacitance divided by the maximum capacitance value at 1 mHz, versus the applied frequency. Normalised capacitance decreased at increasing frequencies, which is related to hindered ion diffusion into the pores at high and medium frequency regimes ($10 - 10^5$ Hz). The frequency response time is given by the relaxation time constant (τ_s), calculated as $1/f_{0.5}$, where $f_{0.5}$ is the frequency at which 50% of the normalised capacitance is achieved. Interestingly, C3/30 exhibited a faster frequency response than F3/30: 4.39 and 8.28 s, respectively. This indicates that the C3/30-based supercapacitor needs less time to charge or discharge 50% of the full charge, likely due to its broader PSD, to its lower oxygen surface content, and to its higher capacitance retention with respect to the F3/30-based electrode. Thus, C3/30 is more appropriate than non-activated OMCs for being used as electrode material in practical devices.

5. Conclusions

Controlling the temperature of self-assembly in the soft-templating synthesis of tannin-derived OMCs is crucial as it allows using milder pH conditions than what was formerly reported, in the absence of formaldehyde or toxic phenolic molecules. The optimal stabilisation of the surfactant-tannin supramolecular structure occurred at pH 3 and 30°C, leading to the material exhibiting the most developed porosity and the most ordered mesostructure and nanotexture. For a given pH value, increasing the temperature from 10 to 30°C decreased the amount of functional groups in the final OMCs, probably due to the lower autocondensation of tannin molecules leading to less compact polymer networks, from which oxygen was more easily released as water during carbonisation. The control of the pH and of the assembly temperature, and the removal of the surfactant at 400°C followed by carbonisation at 900°C, minimised the structural shrinkage and better preserved the mesoporosity. This led to OMCs with similar cell parameters as those produced from thermosetting resorcinol-formaldehyde resins.

Physical activation increased the micropore volume by 58.3% without significantly affecting the structural order, but decreased the mesopore volume and the oxygen content whereas the PSD was slightly broadened in the mesopore range. When used as electrode material in a supercapacitor, the activated OMC evidenced higher gravimetric capacitances (286 F g^{-1} by cyclic voltammetry), higher capacitance retention (50% at 12 A g^{-1}), and higher energy and power densities (17.54 W kg^{-1} and 16.29 kW kg^{-1}, respectively, by galvanostatic charge discharge) than non-activated OMCs and formerly reported hierarchical OMCs. Moreover, the widening of the PSD, the lower oxygen surface concentration and the higher capacitance retention of the activated OMC with respect to the non-activated one allowed decreasing the

frequency response from 8.28 to 4.39 seconds, making the former material more appropriate for practical electrochemical energy storage devices.

ASSOCIATED CONTENT

Electronic Supplementary Information.

Figure S1. (a) TG and DTG curves of F1/10 before carbonisation (dry surfactant–tannin composite material) and mimosa tannin in argon atmosphere; (b) Mass spectrometry profiles of gases evolved from F1/10 before carbonisation *m*/*z* values of 18 (H_2O), 28 (CO + CO_2) and 44 (CO_2).

Figure S2. Nitrogen adsorption isotherms and pore size distributions (PSDs) of the OMCs prepared at 10 °C (a, b) and at 20 °C (c, d), and those of F3/30 carbonised at different temperatures (e, f).

Figure S3. TEM images of F3/10 along the longitudinal direction of the ordered structure.

Figure S4. First-order Raman spectra of the OMCs synthesised at: (a) pH = 1 – 4.5 and T = 10°C; and (b) pH = 1 and T = 10 – 30°C.

Figure S5. C1s high-resolution XPS spectra of representative OMCs.

Figure S6. O1s high-resolution XPS spectra of representative OMCs.

Figure S7. O1s high-resolution XPS spectra of activated OMC.

Figure S8. Possible redox reactions of electroactive oxygen groups in sulphuric acid electrolyte.

Figure S9. Galvanostatic charge-discharge curves (GCD) of the OMCs at a current density of 4 A g^{-1}, measured in the two-electrode cell with 2 mol L^{-1} H_2SO_4 as electrolyte, being the diameter of the electrodes 0.4 cm.

Table S1. Element composition obtained by elemental analysis.

AUTHOR INFORMATION

Corresponding Authors : *A. Sanchez-Sanchez. E-mail: angela.sanchez-sanchez@univ-lorraine.fr. * Vanessa Fierro: vanessa.fierro@univ-lorraine.fr

Author Contributions

The manuscript was written through contributions of all authors. All authors have given approval to the final version of the manuscript.

ACKNOWLEDGMENT

The IJL research team gratefully acknowledges the financial support of the CPER 2007-2013 “Structuration du Pôle de Compétitivité Fibres Grand’Est” (Competitiveness Fibre Cluster), through local (Conseil Général des Vosges), regional (Région Lorraine), national (DRRT and FNADT) and European (FEDER) funds. Part of this work was supported by CHEERS project (FEDER funds). Dr. A. Sanchez-Sanchez acknowledges the University of Lorraine and the Region Lorraine for financing her post-Doctoral contract.

REFERENCES

[1] T. Kyotani, N. Sonobe, A. Tomita, Formation of highly orientated graphite from polyacrylonitrile by using a two-dimensional space between montmorillonite lamellae, Nature. 331 (1988) 331–333. doi:10.1038/331331a0.

[2] Q. Huo, D.I. Margolese, U. Ciesla, P. Feng, T.E. Gier, P. Sieger, R. Leon, P.M. Petroff, F. Schuth, G.D. Stucky, Generalized synthesis of periodic surfactant/inorganic composite materials, Nature. 368 (1994) 317–321. doi:10.1038/368317a0.

[3] W. Li, J. Liu, D. Zhao, Mesoporous materials for energy conversion and storage devices, Nat. Rev. Mater. 1 (2016) 16023. doi:10.1038/natrevmats.2016.23.

[4] Y. Li, Z.-Y. Fu, B.-L. Su, Hierarchically Structured Porous Materials for Energy Conversion and Storage, Adv. Funct. Mater. 22 (2012) 4634–4667. doi:10.1002/adfm.201200591.

[5] E. Frackowiak, F. Beguin, Carbon materials for the electrochemical storage of energy in capacitors, Carbon. 39 (2001) 937–950.

[6] S.H. Joo, S.J. Choi, I. Oh, J. Kwak, others, Ordered nanoporous arrays of carbon supporting high dispersions of platinum nanoparticles, Nature. 412 (2001) 169.

[7] C. Liang, Z. Li, S. Dai, Mesoporous Carbon Materials: Synthesis and Modification, Angew. Chem. Int. Ed. 47 (2008) 3696–3717. doi:10.1002/anie.200702046.

[8] V.G. Bairi, U.B. Nasini, S. Kumar Ramasahayam, S.E. Bourdo, T. Viswanathan, Electrocatalytic and supercapacitor performance of Phosphorous and Nitrogen co-doped Porous Carbons synthesized from Aminated Tannins, Electrochimica Acta. 182 (2015) 987–994. doi:10.1016/j.electacta.2015.10.011.

[9] W. Teng, Z. Wu, J. Fan, W. Zhang, D. Zhao, Amino-functionalized ordered mesoporous carbon for the separation of toxic microcystin-LR, J Mater Chem A. 3 (2015) 19168–19176. doi:10.1039/C5TA05320J.

[10] H. Wang, F.L.Y. Lam, X. Hu, K.M. Ng, Ordered Mesoporous Carbon as an Efficient and Reversible Adsorbent for the Adsorption of Fullerenes, Langmuir. 22 (2006) 4583–4588. doi:10.1021/la052615l.

[11] á. Sánchez-Sánchez, F. Suárez-García, A. Martínez-Alonso, J.M.D. Tascón, Synthesis, characterization and dye removal capacities of N-doped mesoporous carbons, J. Colloid Interface Sci. 450 (2015) 91–100. doi:10.1016/j.jcis.2015.02.073.

[12] B. Yuan, X. Wu, Y. Chen, J. Huang, H. Luo, S. Deng, Adsorption of CO_2, CH_4, and N_2 on Ordered Mesoporous Carbon: Approach for Greenhouse Gases Capture and Biogas Upgrading, Environ. Sci. Technol. 47 (2013) 5474–5480. doi:10.1021/es4000643.

[13] Á. Sánchez-Sánchez, T.A. Centeno, F. Suárez-García, A. Martínez-Alonso, J.M.D. Tascón, The importance of electrode characterization to assess the supercapacitor performance of ordered mesoporous carbons, Microporous Mesoporous Mater. 235 (2016) 1–8. doi:10.1016/j.micromeso.2016.07.052.

[14] G. Lin, F. Wang, Y. Wang, H. Xuan, R. Yao, Z. Hong, X. Dong, Enhanced electrochemical performance of ordered mesoporous carbons by a one-step carbonization/activation treatment, J. Electroanal. Chem. 758 (2015) 39–45. doi:10.1016/j.jelechem.2015.10.016.

[15] M. Inagaki, H. Konno, O. Tanaike, Carbon materials for electrochemical capacitors, J. Power Sources. 195 (2010) 7880–7903. doi:10.1016/j.jpowsour.2010.06.036.

[16] S. Oh, K. Kim, others, Synthesis of a new mesoporous carbon and its application to electrochemical double-layer capacitors, Chem. Commun. (1999) 2177–2178.

[17] J.R. Miller, P. Simon, MATERIALS SCIENCE: Electrochemical Capacitors for Energy Management, Science. 321 (2008) 651–652. doi:10.1126/science.1158736.

[18] D.M. Anjos, J.K. McDonough, E. Perre, G.M. Brown, S.H. Overbury, Y. Gogotsi, V. Presser, Pseudocapacitance and performance stability of quinone-coated carbon onions, Nano Energy. 2 (2013) 702–712. doi:10.1016/j.nanoen.2013.08.003.

[19] P. Simon, Y. Gogotsi, B. Dunn, Where Do Batteries End and Supercapacitors Begin?, Science. 343 (2014) 1210–1211. doi:10.1126/science.1249625.

[20] P. Simon, Y. Gogotsi, Materials for electrochemical capacitors, Nat. Mater. 7 (2008) 845–854.

[21] A.-H. Lu, F. Schüth, Nanocasting: A Versatile Strategy for Creating Nanostructured Porous Materials, Adv. Mater. 18 (2006) 1793–1805. doi:10.1002/adma.200600148.

[22] L. Chuenchom, R. Kraehnert, B.M. Smarsly, Recent progress in soft-templating of porous carbon materials, Soft Matter. 8 (2012) 10801. doi:10.1039/c2sm07448f.

[23] S. Tanaka, N. Nishiyama, Y. Egashira, K. Ueyama, Synthesis of ordered mesoporous carbons with channel structure from an organic–organic nanocomposite, Chem Commun. (2005) 2125–2127. doi:10.1039/B501259G.

[24] Y. Deng, T. Yu, Y. Wan, Y. Shi, Y. Meng, D. Gu, L. Zhang, Y. Huang, C. Liu, X. Wu, D. Zhao, Ordered Mesoporous Silicas and Carbons with Large Accessible Pores Templated from Amphiphilic Diblock Copolymer Poly(ethylene oxide)- *b* -polystyrene, J. Am. Chem. Soc. 129 (2007) 1690–1697. doi:10.1021/ja067379v.

[25] D. Long, W. Qiao, L. Zhan, X. Liang, L. Ling, Effect of template and precursor chemistry on pore architectures of triblock copolymer-templated mesoporous carbons, Microporous Mesoporous Mater. 121 (2009) 58–66. doi:10.1016/j.micromeso.2009.01.003.

[26] D. Saha, K.E. Warren, A.K. Naskar, Soft-templated mesoporous carbons as potential materials for oral drug delivery, Carbon. 71 (2014) 47–57. doi:10.1016/j.carbon.2014.01.005.

[27] P. Schofield, D.M. Mbugua, A.N. Pell, Analysis of condensed tannins: a review, Tann. Anal. Biol. Eff. Rumin. Feeds. 91 (2001) 21–40. doi:10.1016/S0377-8401(01)00228-0.

[28] F.L. Braghiroli, V. Fierro, J. Parmentier, A. Pasc, A. Celzard, Easy and eco-friendly synthesis of ordered mesoporous carbons by self-assembly of tannin with a block copolymer, Green Chem. 18 (2016) 3265–3271. doi:10.1039/C5GC02788H.

[29] K.M. Nelson, S.M. Mahurin, R.T. Mayes, B. Williamson, C.M. Teague, A.J. Binder, L. Baggetto, G.M. Veith, S. Dai, Preparation and CO 2 adsorption properties of soft-templated mesoporous carbons derived from chestnut tannin precursors, Microporous Mesoporous Mater. 222 (2016) 94–103. doi:10.1016/j.micromeso.2015.09.050.

[30] J. Jagiello, J.P. Olivier, 2D-NLDFT adsorption models for carbon slit-shaped pores with surface energetical heterogeneity and geometrical corrugation, Carbon. 55 (2013) 70–80. doi:10.1016/j.carbon.2012.12.011.

[31] M. Pawlyta, J.-N. Rouzaud, S. Duber, Raman microspectroscopy characterization of carbon blacks: Spectral analysis and structural information, Carbon. 84 (2015) 479–490. doi:10.1016/j.carbon.2014.12.030.

[32] X. Wang, C. Liang, S. Dai, Facile Synthesis of Ordered Mesoporous Carbons with High Thermal Stability by Self-Assembly of Resorcinol−Formaldehyde and Block Copolymers under Highly Acidic Conditions, Langmuir. 24 (2008) 7500–7505. doi:10.1021/la800529v.

[33] S. Jun, S.H. Joo, R. Ryoo, M. Kruk, M. Jaroniec, Z. Liu, T. Ohsuna, O. Terasaki, Synthesis of New, Nanoporous Carbon with Hexagonally Ordered Mesostructure, J. Am. Chem. Soc. 122 (2000) 10712–10713. doi:10.1021/ja002261e.

[34] M. Thommes, K.A. Cychosz, A.V. Neimark, Chapter 4 - Advanced Physical Adsorption Characterization of Nanoporous Carbons A2 - Tascón, Juan M.D., in: Nov. Carbon Adsorbents, Elsevier, Oxford, 2012: pp. 107–145. doi:10.1016/B978-0-08-097744-7.00004-1.

[35] A. Sanchez-Sanchez, M.T. Izquierdo, J. Ghanbaja, G. Medjahdi, S. Mathieu, A. Celzard, V. Fierro, Excellent electrochemical performances of nanocast ordered mesoporous carbons based on tannin-related polyphenols as supercapacitor electrodes, J. Power Sources. 344 (2017) 15–24. doi:10.1016/j.jpowsour.2017.01.099.

[36] F.L. Braghiroli, V. Fierro, J. Parmentier, L. Vidal, P. Gadonneix, A. Celzard, Hydrothermal carbons produced from tannin by modification of the reaction medium: Addition of H + and Ag +, Ind. Crops Prod. 77 (2015) 364–374. doi:10.1016/j.indcrop.2015.09.010.

[37] S. Schlienger, A.-L. Graff, A. Celzard, J. Parmentier, Direct synthesis of ordered mesoporous polymer and carbon materials by a biosourced precursor, Green Chem. 14 (2012) 313–316. doi:10.1039/C2GC16160E.

[38] A. Arbenz, L. Avérous, Chemical modification of tannins to elaborate aromatic biobased macromolecular architectures, Green Chem. 17 (2015) 2626–2646. doi:10.1039/C5GC00282F.

[39] U.H.B. Abdullah, A. Pizzi, Tannin-furfuryl alcohol wood panel adhesives without formaldehyde, Eur. J. Wood Wood Prod. 71 (2013) 131–132. doi:10.1007/s00107-012-0629-4.

[40] N. Meikleham, A. Pizzi, A. Stephanou, Induced accelerated autocondensation of polyflavonoid tannins for phenolic polycondensates. I. 13C-NMR, 29Si-NMR, X-ray, and polarimetry studies and mechanism, J. Appl. Polym. Sci. 54 (1994) 1827–1845.

[41] A.C. Ferrari, Raman spectroscopy of graphene and graphite: Disorder, electron–phonon coupling, doping and nonadiabatic effects, Solid State Commun. 143 (2007) 47–57. doi:10.1016/j.ssc.2007.03.052.

[42] A.C. Ferrari, J. Robertson, Interpretation of Raman spectra of disordered and amorphous carbon, Phys. Rev. B. 61 (2000) 14095.

[43] V.N. Tsaneva, W. Kwapinski, X. Teng, B.A. Glowacki, Assessment of the structural evolution of carbons from microwave plasma natural gas reforming and biomass pyrolysis using Raman spectroscopy, Carbon. 80 (2014) 617–628. doi:10.1016/j.carbon.2014.09.005.

[44] R.E. Franklin, Crystallite growth in graphitizing and non-graphitizing carbons, in: Proc. R. Soc. Lond. Math. Phys. Eng. Sci., The Royal Society, 1951: pp. 196–218. http://rspa.royalsocietypublishing.org/content/209/1097/196.short (accessed February 6, 2017).

[45] F. Braghiroli, V. Fierro, A. Pizzi, K. Rode, W. Radke, L. Delmotte, J. Parmentier, A. Celzard, Reaction of condensed tannins with ammonia, Ind. Crops Prod. 44 (2013) 330–335. doi:10.1016/j.indcrop.2012.11.024.

[46] D.L. Perry, A. Grint, Application of XPS to coal characterization, Fuel. 62 (1983) 1024–1033.

[47] J.P. Boudou, P. Parent, F. Suárez-García, S. Villar-Rodil, A. Martínez-Alonso, J.M.D. Tascón, Nitrogen in aramid-based activated carbon fibers by TPD, XPS and XANES, Carbon. 44 (2006) 2452–2462. doi:10.1016/j.carbon.2006.04.036.

[48] D. Briggs, Surface Analysis of Polymers by XPS and Static SIMS, Cambridge University Press, 1998.

[49] S. Tanaka, H. Fujimoto, J.F.M. Denayer, M. Miyamoto, Y. Oumi, Y. Miyake, Surface modification of soft-templated ordered mesoporous carbon for electrochemical supercapacitors, Microporous Mesoporous Mater. 217 (2015) 141–149. doi:10.1016/j.micromeso.2015.06.017.

[50] X. Liu, T. Osaka, Properties of Electric Double-Layer Capacitors with Various Polymer Gel Electrolytes, J. Electrochem. Soc. 144 (1997) 3066–3071.

[51] C.-T. Hsieh, H. Teng, Influence of oxygen treatment on electric double-layer capacitance of activated carbon fabrics, Carbon. 40 (2002) 667–674.

[52] T. Momma, X. Liu, T. Osaka, Y. Ushio, Y. Sawada, Electrochemical modification of active carbon fiber electrode and its application to double-layer capacitor, J. Power Sources. 60 (1996) 249–253.

[53] A.G. Pandolfo, A.F. Hollenkamp, Carbon properties and their role in supercapacitors, J. Power Sources. 157 (2006) 11–27. doi:10.1016/j.jpowsour.2006.02.065.

[54] J.A. Fernández, S. Tennison, O. Kozynchenko, F. Rubiera, F. Stoeckli, T.A. Centeno, Effect of mesoporosity on specific capacitance of carbons, Carbon. 47 (2009) 1598–1604. doi:10.1016/j.carbon.2009.02.012.

[55] A. Yoshida, I. Tanahashi, A. Nishino, Effect of concentration of surface acidic functional groups on electric double-layer properties of activated carbon fibers, Carbon. 28 (1990) 611–615.

Insert Table of Contents Graphic and Synopsis Here